Research Article

Aerodynamics and countermeasures of train-tail swaying inside single-line tunnels

Yadong SONG[1], Yanpeng ZOU[2], Yuan YAO[1,3][✉], Ting QIN[1], Longjiang SHEN[3]

[1]*State Key Laboratory of Rail Transit Vehicle System, Southwest Jiaotong University, Chengdu 610031, China*
[2]*Foundation Service Department of CRRC Changke Co., Ltd, Changchun 130062, China*
[3]*State Key Laboratory of Heavy-duty and Express High-power Electric Locomotive,CRRC Zhuzhou Electric Locomotive Co., Ltd, Zhuzhou 412000, China*

Abstract: In recent years, train-tail swaying of 160 km/h EMUs inside single-line tunnels has been heavily researched, because the issue needs to be solved urgently. In this paper, a co-simulation model of vortex-induced vibration (VIV) of the tail carbody is established, and the aerodynamics of train-tail swaying is studied. The simulation results were confirmed through a field test of operating EMUs. Furthermore, the influence mechanism of train-tail swaying on the wake flow field is studied in detail through a wind-tunnel experiment and a simulation of a reduced-scaled train model. The results demonstrate that the aerodynamic force frequency (i.e., vortex-induced frequency) of the train tail increases linearly with train speed. When the train runs at 130 km/h, with a small amplitude of train-tail swaying (within 10 mm), the vortex-induced frequency is 1.7 Hz, which primarily depends on the nose shape of the train tail. After the tail carbody's nose is extended, the vortex-induced frequency is decreased. As the swaying amplitude of the train tail increases (exceeding 25 mm), the separation point of the high-intensity vortex in the train wake shifts downstream to the nose tip, and the vortex-induced frequency shifts from 1.7 Hz to the nearby carbody hunting (i.e., the primary hunting) frequency of 1.3 Hz, which leads to the frequency-locking phenomenon of VIV, and the resonance intensifies train-tail swaying. For the motor vehicle of the train tail, optimization of the yaw damper to improve its primary hunting stability can effectively alleviate train-tail swaying inside single-line tunnels. Optimization of the tail-carbody nose shape reduces the amplitude of the vortex-induced force, thereby weakening the aerodynamic effect and solving the problem of train-tail swaying inside the single-line tunnels.

Key words: Train-tail swaying; Vortex-induced vibration; Wake flow field; Train aerodynamics; Vehicle dynamics

1 Introduction

1.1 Engineering background

In China, since power-concentrated EMUs (Electric Multiple Units) with a speed level of 160 km/h were put into operation in Jan 2019, some of the vehicles have exhibited lateral dynamics issues. In addition to the lack of hunting stability on local lines (Shi *et al*., 2020; Sun *et al*., 2021; Li *et al*., 2022), there is a discrepancy in the lateral ride index between the two ends of the locomotive (Li *et al*., 2023), and the deterioration of lateral ride comfort caused by continuous swaying of the train tail inside single-line tunnels is particularly serious (Yao *et al*., 2021). When EMUs pass through a single-line tunnel, the constant swaying of the tail carbody is obvious, which has attracted the attention of relevant railway departments. As the phenomenon only occurs inside tunnels, it has been suggested that it is not associated with track irregularities or self-induced hunting motion, but is caused by the external aerodynamics of the train wake.

According to our on-track tests and simulation analysis of actual operating EMUs, train-tail swaying only occurs within a specific speed range of 120–130 km/h, and the phenomenon disappears as train speed increases. Therefore, it is not a result of negative

✉ Yuan YAO, yyuan8848@163.com

Yadong SONG, https://orcid.org/0000-0002-4809-7329
Yuan YAO, https://orcid.org/0000-0003-2279-7463

damping vibration; the aerodynamic effects of galloping and flutter are thus excluded, and vortex-induced vibration (VIV) is obviously more reasonable as a cause. To address this practical problem, it is necessary to clarify the relevant mechanism and propose corresponding solutions.

1.2 Review of related research

Train swaying inside tunnels was initially discovered in the 1990s in Japan. The carbody's lateral swaying was most noticeable on the Shinkansen, and it gradually increased from the front vehicle to the rear vehicle of the train (Fujimoto *et al*., 1993). The swaying of train tails inside tunnels has been a subject of numerous studies. Takai (1990) first proposed that the aerodynamic load inside tunnels was the primary cause and that track disturbance had little impact. Earlier studies (Suzuki *et al*., 2000a; 2001b; 2004c) by the RTRI (Railway Technical Research Institute) in Japan also showed that a propagation pressure disturbance (PPD) was generated alongside the carbody in the tunnel, and was strong enough to negatively impact ride comfort. Diedrichs *et al*. (2007a; 2008b) studied the aerodynamic response of the tail carbody of the Japanese S300 and German ICE2 trains inside tunnels using large eddy simulation (LES). They found that flow separation caused vibration of the tail carbody, leading to a linear increase in pressure disturbance from the nose to around 150–200 m downstream. Based on carbody pressure data measured inside tunnels, Tanifuji and Kikko (2008) developed a mathematical model to study the ride comfort of trains under an aerodynamic load in tunnels.

As the running speed of railway vehicles increases, it inevitably leads to deterioration of aerodynamic performance. Over the past decade, computational fluid dynamics (CFD) and wind-tunnel tests have advanced rapidly, and many scholars have conducted more in-depth research on the aerodynamic performance of railway vehicles. Choi *et al*. (2014) used CFD simulation to study the effect of train-nose length and tunnel cross-sectional area on a carbody's aerodynamic drag in tunnels. Niu *et al*. (2016a; 2017b; 2018c) studied the aerodynamic force

of a CRH380A train under different operating conditions through numerical simulation and wind-tunnel tests on a reduced-scale train model. Zeng *et al*. (2014a; 2018b) analyzed the carbody hunting performance of a high-speed train under constant aerodynamic load by numerical simulation. Pan *et al*. (2018) studied the wake vortex structure of a high-speed train by vortex identification methods, and found that powerful vortices with high vorticity magnitude mostly appeared near the tail car. Through numerical modeling, Du *et al*. (2022) explored how the number of cars affected both aerodynamic pressure and micropressure waves in a tunnel. Wang *et al*. (2022) studied the effect of wheel-rail contact characteristics and aerodynamic forces on carbody hunting performance. Li *et al*. (2021a; 2023b) conducted extensive research on aerodynamic resistance during train operation, and used a vortex generator (VG) to reduce the tail carbody's aerodynamic resistance in a ICE2 high-speed train.

Vortex-induced vibration (VIV) is a classic fluid-structure interaction (FSI) phenomenon, which is caused by the vibration of fluid coupled to the elastic system (Han *et al*., 2023; Williamson *et al*., 2004). At present, the research on vortex-induced vibration (VIV) theory is mainly focused on structures with slender appearance such as marine pipelines and large-span bridges, and much progress has been made (Yu *et al*., 2023; Zhang *et al*., 2023; Zhao *et al*., 2023). VIV occurs when the vortex-induced frequency approaches a certain natural frequency of the structure, and the frequency of vortex-induced force is "locked" on that natural frequency at the same time (Liu *et al*., 2022). The significant difference between a train and other ground vehicles is that a train has a large slenderness ratio in terms of fluid mechanics. The flow of air surrounding the train is also distinct from that of airplanes, owing to its interaction with the ground. The flow field around a train is basically 3-D turbulent flow because of its geometric features and running speed (Khier *et al*., 2000). Due to the imperfection of vibration theory, it is helpful to study vortex-induced vibration through wind-tunnel tests (Zhou *et al*., 2008). Bell *et al*. (2014a; 2015b; 2016c) analyzed the slipstream and wake of an ICE3 high-speed train with a 1/10th-scale wind-tunnel ex-

periment. Hemida and Krajnovic (2009a; 2010b) discovered that there was a certain relationship between carbody vibration and the vortex-induced frequency of a train's wake.

1.3 Motivation of this study

The main questions that motivated this study are:

1. How do aerodynamic forces cause the tail of 160 km/h EMUs to continuously sway inside single-line tunnels, leading to a deterioration in ride comfort?

2. What is the magnitude and corresponding frequency of the aerodynamic force that causes train-tail swaying inside single-line tunnels, and what is the vibration frequency of train-tail swaying?

3. What effective measures can be taken to alleviate the swaying phenomenon of the EMU tail inside single-line tunnels?

The scope of this study draws attention to a relatively new topic, namely the carbody vibration induced by aerodynamics that ultimately affects ride comfort through vehicle dynamics.

During actual train operation, the swaying of the tail carbody interacts with the wake flow field, and the aerodynamic force generated by the train wake is unsteady. Therefore, it was necessary for us to carry out transient analysis of fluid-structure interaction. As far as we know, the majority of previous studies applied the calculated aerodynamic force as the constant excitation to the carbody, while a minority focused on assessing carbody vibration with regard to fluid-structure interaction. Regrettably, little research has been done on how VIV affects a vehicle system's aerodynamic performance. These were additional challenges for us in carrying out this research.

1.4 Contributions and structure of this paper

In this paper, we establish a co-simulation model for the vortex-induced vibration (VIV) of a 160 km/h EMU tail in a single-track tunnel, and clarify the mechanism of train-tail swaying caused by vortex-induced vibration; this is verified by experiments. Finally, we propose effective measures to alleviate the problem of train-tail swaying in single-line tunnels by optimizing vehicle suspension and tail nose shape.

The rest of this paper is structured as follows. In Section 2, the technical route, research methodology,

and train-tail fluid-structure coupled dynamics model are introduced. In Section 3, the aerodynamic force of the train tail is analyzed, and the swaying mechanism of VIV is investigated. In Section 4, we describe the on-track tests used to verify the simulation results, as well as how we further analyzed the surface pressure and flow-field characteristics around the tail carbody with a reduced-scale model of the train and wind-tunnel experiments. In section 5, we discuss the countermeasures for optimizing vehicle suspension and tail nose shape. The paper ends with some conclusions and ideas for future research, in Section 6.

2 Methodology

2.1 Technical route

In order to study train-tail swaying of 160km/h EMUs in a single-line tunnel, we adopted a combination of simulation and experimental methods; the specific technical route is shown in Fig. 1. The key to the simulation method was to establish the fluid-structure coupled simulation platform, which analyzed the flow characteristics of the train wake and the dynamic performance of the tail vehicle. The key aspects of the experimental method were constructing a wind-tunnel test bench for a 1/25-scale train model, and conducting on-track tests of the actual running train. We then verified the simulation results with experiments. Finally, through simulation analysis, we were able to determine effective measures to alleviate train-tail swaying inside tunnels.
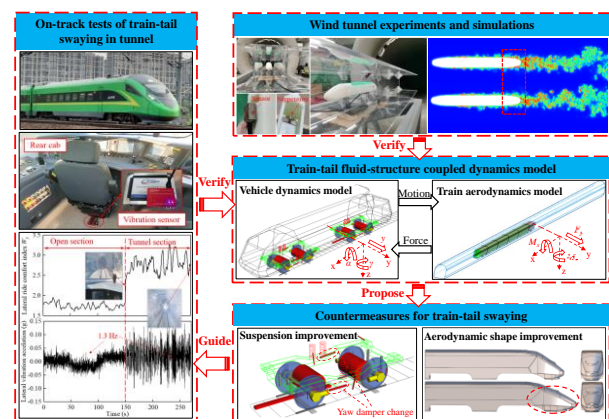

Fig. 1 Research flow of this study

There are two main methods of fluid-structure coupled calculation: the partitioned method and the

monolithic method. We used the partitioned method, which solves the flow field and dynamics separately. The simulation of train-tail swaying in the tunnel was based on the vehicle dynamics model and train aerodynamics model shown in Fig. 2a, and the specific coupled calculation flow is shown in Fig. 2b. The specific calculation process was illustrated in detail in our recent study (Song *et al.* 2023). In addition, the consistent time-step Δt and the number of steps n employed in the following transient simulation were 0.05 ms and 800×10^3, respectively.

(a)

(b)
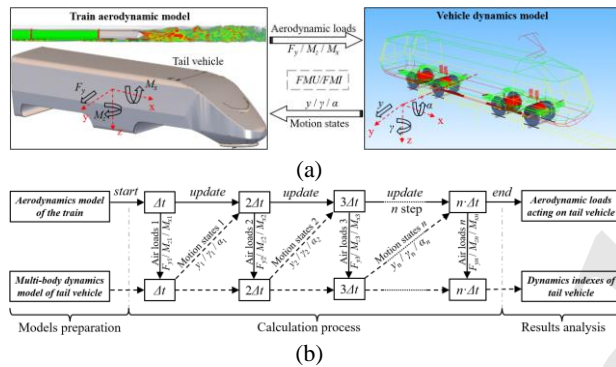
Fig. 2 Fluid-structure coupled simulation for train-tail vibration: (a) model; (b) flowchart

2.2 Vehicle dynamics sub-model

The dynamics model of the 160 km/h EMU tail motor vehicle was developed in SIMULIA Simpack 2020. The whole vehicle multi-body system has 25 rigid bodies and 90 degrees of freedom. For the vehicle suspension system, the secondary suspension consists of a yaw damper, secondary lateral/vertical damper, and flex-coil spring; the primary suspension consists of an axle box spring, a rotating arm, and primary vertical dampers, as shown in Fig. 3. Moreover, all dampers are based on the Maxwell model, the wheel/rail functions are constructed with the CN60 rail and JM3 wheel profiles, and the track irregularity is based on the irregularity described in Li *et al.* (2014). Our other related papers (Li *et al.*, 2022; Song *et al.* 2023) list the main dynamic parameters and structures of the motor vehicle, and also describe how we confirmed the accuracy and reliability of the Simpack model.
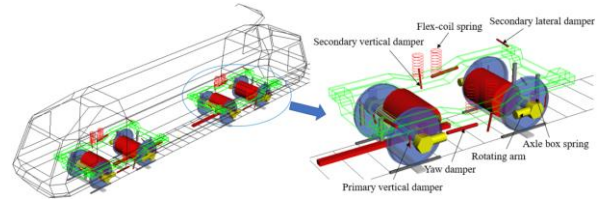
Fig. 3 Dynamics model of the motor vehicle

2.3 Train aerodynamics sub-model

The CFD model of the train aerodynamics simulation inside a tunnel was established in SIMULIA XFlow 2021x, and was based on the particle method. We used a 160 km/h EMU for numerical simulations (see Fig. 4). The train model is simplified according to the CEN standard (2009a; 2010b), and the shape of the single-line tunnel is based on the standard of GB 146.2 (2020). The train height H, also known as the characteristic length in train aerodynamics, is 4.0 m at 1:1 scale.

(a)

(b)
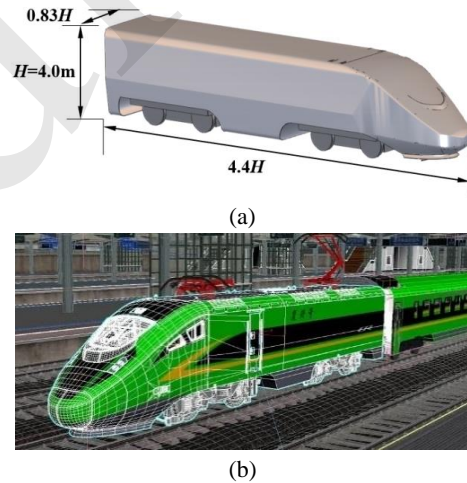
Fig. 4 160 km/h EMU models in this study: (a) train model employed in numerical simulations; (b) actual train

The aerodynamics model of a train running inside a single-line tunnel is illustrated in Fig. 5. The train is located at a distance of 20H from the tunnel inlet and 45H from the tunnel outlet, which prevents the influence of boundary conditions on the flow field around the train referring to the EN 14067-6 standard (2018). The tunnel inlet is defined as the velocity inlet boundary condition, and the inlet velocity U is the train speed along the x-axis. The tunnel outlet is defined as the pressure-outlet boundary condition, with

a reference pressure of 0 Pa. The train's surface and the tunnel's inner wall are defined as the non-equilibrium enhanced wall-function in XFlow (SIMULIA Xflow, 2021). The Reynolds number *Re* in this simulation is about 8.1×10^6, and the formula is as follows.

$$Re = \rho U H / \mu. \qquad (1)$$

Considering that the on-track tests in Section 4 were conducted in an area with high elevation, the air density ρ is set to 1.01 kg/m³, and the air viscosity parameter μ is set to 17.9×10^{-6} Pa s. In addition, the train speed *U* is 36 m/s (130 km/h) in the tunnel.
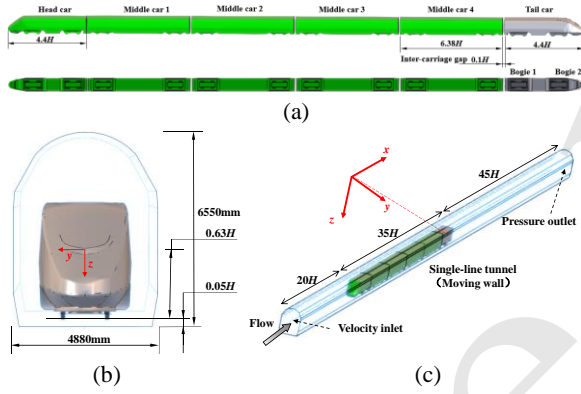
Fig. 5 Train and tunnel aerodynamics model at full scale: (a) side view; (b) elevation view; (c) domain and boundaries of computation

In the numerical simulation, the calculated particle is the octree lattice structure of the D3Q27 organization constructed by XFlow according to the given geometry (SIMULIA Xflow, 2021). The calculated particle distribution of the computational domain is illustrated in the Electronic Supplementary Materials (ESM), and the accuracy of the train aerodynamics model has been proved in our recent research (Song *et al*. 2023), which is not illustrated here.

3 Simulation

3.1 Calculated conditions

On an actual railway line, the track operation environment in tunnels is relatively poor and maintenance is difficult. In order to simulate the coupling vibration caused by EMU tail swaying in a single-line tunnel, three kinds of line conditions are set in this section, corresponding to three different scales of track irregularity:

Cond 1: smooth line, with no track irregularity;
**Cond 2**: normal line, with track irregularity;
Cond 3: poor line, with the amplitude of track lateral irregularity doubled
where the track irregularity is obtained by high-speed track spectrum (Li *et al*., 2014). The lateral irregularity is shown in the ESM. In addition, the simulation time is set to 40 s, the vehicle speed is 130 km/h, and other parameters are as introduced in Section 2.

3.2 Aerodynamic performance analysis

According to a recent study by Song *et al*. (2023), the time-frequency variation of aerodynamic moment M_x, M_z and force F_y acting on a tail carbody is almost the same, and is dominated by the vortex-induced frequency of the train wake. Therefore, we only analyzed the lateral movement *y* of the tail carbody and the typical vortex-induced force F_y under three conditions, as shown in Figs. 6 and 7, respectively.

These figures demonstrate that with increasing lateral movement *y* of the train tail, the vortex-induced force F_y also changes. In Cond 1, when the amplitude of the train tail is within 10 mm, the dominant frequency of F_y is 1.7 Hz, corresponding to the vortex-induced frequency of the train wake (Schulte *et al*., 2003). Furthermore, the vortex-induced frequency is related to tail shape and train speed, which is explained in detail in Sections 4 and 5. As the amplitude of *y* increases, the amplitude of F_y slightly increases, while its dominant frequency significantly shifts from 1.7 Hz to 1.3 Hz. In Cond 3, when the amplitude of the train tail increases to 25 mm, the frequency of F_y is dominated by 1.3 Hz, which is the carbody hunting frequency at 130 km/h, as verified in Section 3.
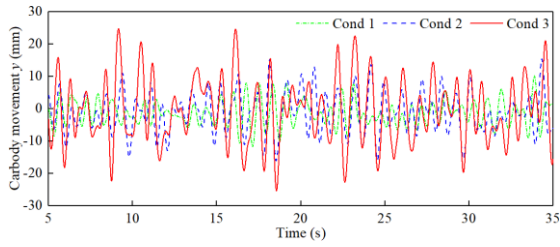
Fig. 6 The lateral movement of the train tail

(a)

(b)
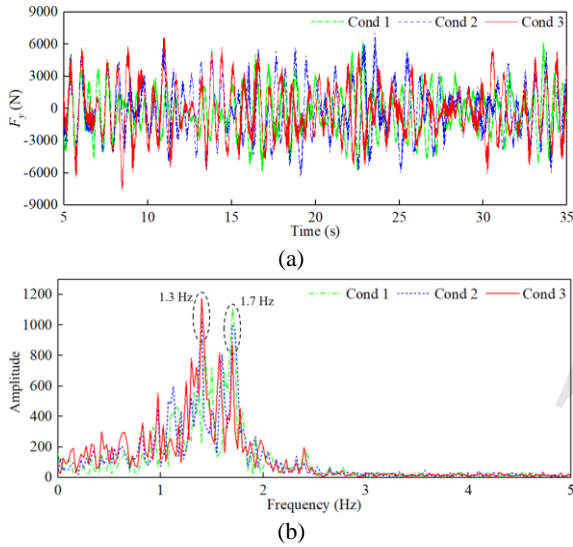
Fig. 7 Vortex-induced force F_y of the train tail: (a) time domain; (b) frequency domain

In fluid mechanics, the dimensionless frequency *St* (Strouhal number) is commonly used. It relates the vortex-induced frequency to the flow velocity and characteristic size of the object, and is defined as follows:

$$St = f_{st} \cdot H / U. \qquad (2)$$

where f_{st} represents the vortex-induced frequency of the stationary object. In this study, the corresponding f_{st} of the train tail is 1.7 Hz, and the calculated *St* is about 0.188.

In addition, Suzuki (2004) has found that small vibration of a tail carbody has little effect on the train wake, while large vibration affects the aerodynamic force; but they did not conduct in-depth research on this subject. Here, for the EMU operating at 130 km/h inside a single-line tunnel, the vortex-induced frequency of the train wake is 1.7 Hz, which approaches 1.3 Hz of the carbody hunting frequency.

As the swaying amplitude of the train tail increases, the vortex-induced frequency shifts from 1.7 Hz to 1.3 Hz, and VIV resonance of occurs.

3.3 Analysis of wake characteristics

The vortex around the train tail is powerful (with high vorticity), and it falls off in pairs from the tail nose to the downstream, in a similar fashion to the Karman vortex street. As time progresses, the train wake turns into fully developed turbulent vortices. The train wake is an intensive turbulent flow with remarkable unsteadiness, and the aerodynamic force of the tail vehicle is severely affected by the generation, evolution, and collapse of wake vortices (Yao *et al*., 2013).

Fig. 8 shows the wake vortex structure of the EMU running in a single-line tunnel, as detected from the Q criterion, in which Q is dimensionless by $(U/H)^2$, with values of 0.1, 0.05, 0.01, and 0.001. It can be observed that high-intensity vortices of the train wake are well captured by the Q criterion. Meanwhile, with higher values of Q, the high-intensity vortex separated from the shear layer of the train-tail surface is more clearly shown, and the low-intensity vortex in the train wake gradually appears. In addition, the initial vortices separated from the tail nose can be divided into two major vortex structures (V1 and V2) on both sides of the train tail; these are described in detail below.
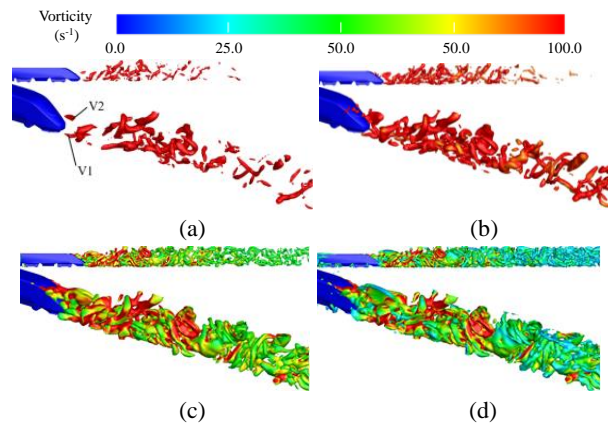

Fig. 8 Wake vortex structures inside the tunnel with various Q values (Cond 2, t = 19 s):
(a) Q = 0.1; (b) Q = 0.05; (c) Q = 0.01; (d) Q = 0.001

To further illustrate the variation law of tail

aerodynamic force (i.e., vortex-induced force) with train-wake development, we analyzed a complete cycle of the vortex evolution in the train wake under Cond 2. We also obtained the instantaneous vorticity contours at 10 different times, where are on the vertical section positioned $x = 0.5H$ downstream from the nose tip of the train tail, as shown in Fig. 9.
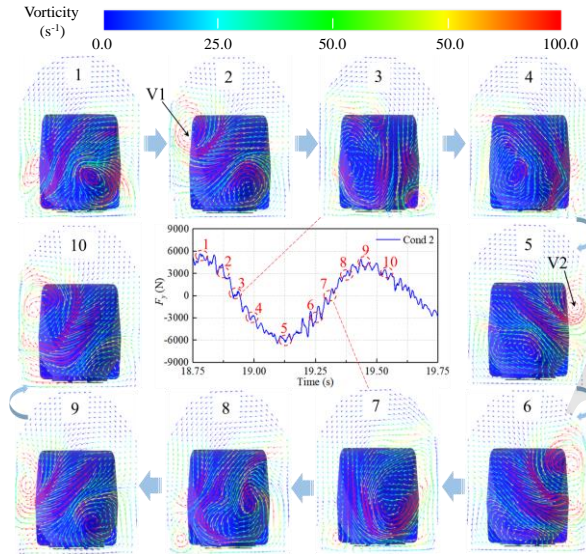

Fig. 9 Cycle of the vortex evolution in the train wake (Cond 2, at $x = H$)

One can see from Fig. 9 that a pair of counter-rotating streamwise vortices alternately appear in the train wake, and with the evolution of the vortex, the aerodynamic force F_y changes periodically. At time 1 and time 2, the clockwise vortex V1 on the left side of the train tail is the most significant, that is, the vortex core with high vorticity appears, and the aerodynamic force reaches its maximum. Subsequently, vortex V1 dissipates, and the aerodynamic force gradually decreases, as shown at time 3. Then, counterclockwise vortex V2 on the right side of the train tail begins to appear, and the aerodynamic force gradually increases in reverse. At time 5 and time 6, when vortex V2 becomes the most significant, the aerodynamic force reaches the reverse maximum. Meanwhile, there is a tendency for the dominant vortex V2 to separate into another reverse vortex V1 on the other side. Through this cycle, the periodic aerodynamic force caused by wake vortex-shedding is formed.

4 Validation

4.1 On-track tests

The real-time aerodynamic force acting on the carbody during train operation is difficult to measure, unlike the acceleration response of the carbody under aerodynamic force. In order to obtain the vibration characteristics of the train tail inside a single-line tunnel, our study team conducted on-track tests on the Yuxi-Mengzi line of Yunnan, China, in Nov 2022.
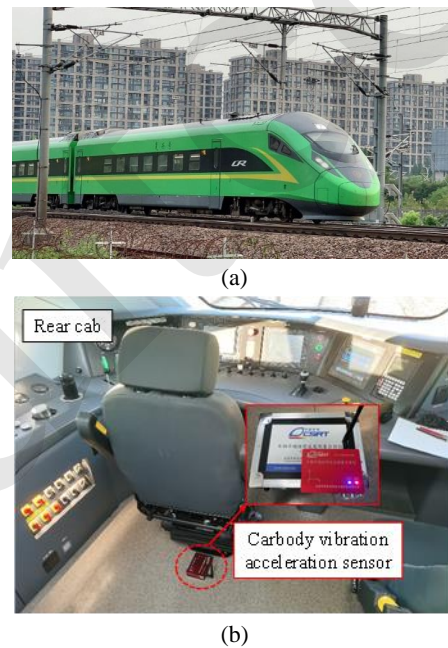

Fig. 10 Tested train: (a) the 160 km/h EMUs; (b) vibration measurement of the EMU tail

In the tests, the train speed was approximately 130 km/h. As shown in Fig. 10b, the vibration of the EMU tail was analyzed, and a carbody acceleration sensor was placed on the rear cab of the train tail. As in GB/T5599 (2019), we used the lateral ride index W_y calculated by carbody acceleration. The W_y value of less than 2.75 indicates excellent lateral ride comfort for a motor vehicle, as illustrated in the ESM.

Fig. 11 shows the lateral vibration results for the train entering a single-line tunnel at 130 km/h. It can be seen that in the open section, the acceleration of the train tail was within 0.05 g, and the W_y was less than 2.75. After entering the tunnel, the lateral vibration of the train tail rapidly increased to an amplitude of

about 0.12 g, and ride comfort deteriorated sharply, with a maximum W_y of 3.3.

(a)

(b)
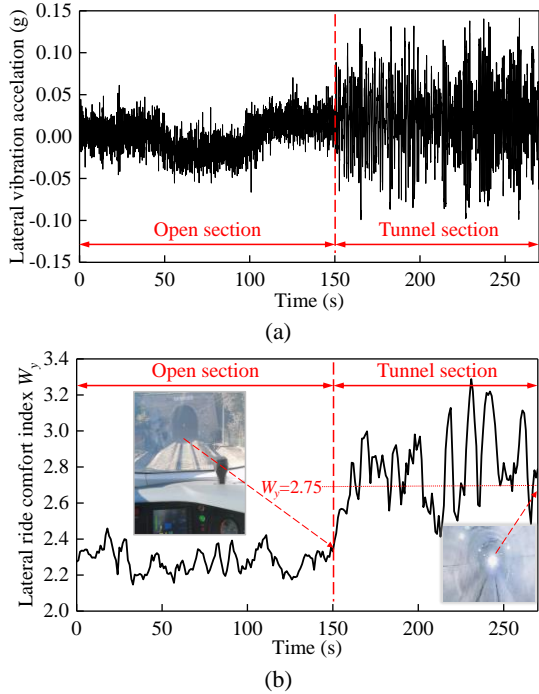
Fig. 11 Test results for a train entering a single-line tunnel: (a) lateral acceleration; (b) lateral ride comfort

Next, we conducted frequency-domain analysis of the carbody lateral acceleration. As shown in Fig. 12a, the dominant frequency of the lateral vibration of the train tail was 1.3 Hz in the open section, which represents the carbody hunting frequency at 130 km/h. Furthermore, when the train tail vibrated violently under the aerodynamic force in the tunnel section, the swaying frequency of the train tail remained around 1.3 Hz of its natural frequency, as shown in Fig. 12b.

(a)

(b)
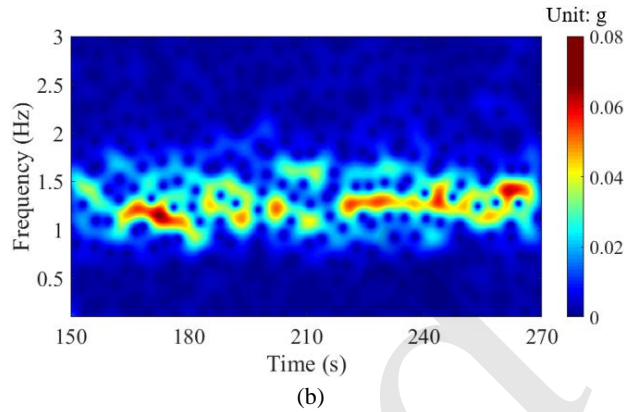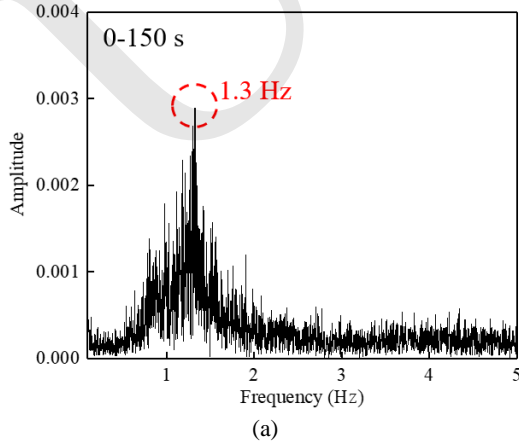
Fig. 12 Frequency-domain analysis of carbody lateral acceleration: (a) open section; (b) tunnel section

4.2 Wind-tunnel experiment

Because of the limitations of the full-scale vehicle experiment, we decided to study the aerodynamic characteristics of the train tail through a wind-tunnel experiment on a reduced-scale train model. This experiment was conducted in the Aerodynamics Laboratory of Southwest Jiaotong University in May 2023.

(a)

(b)
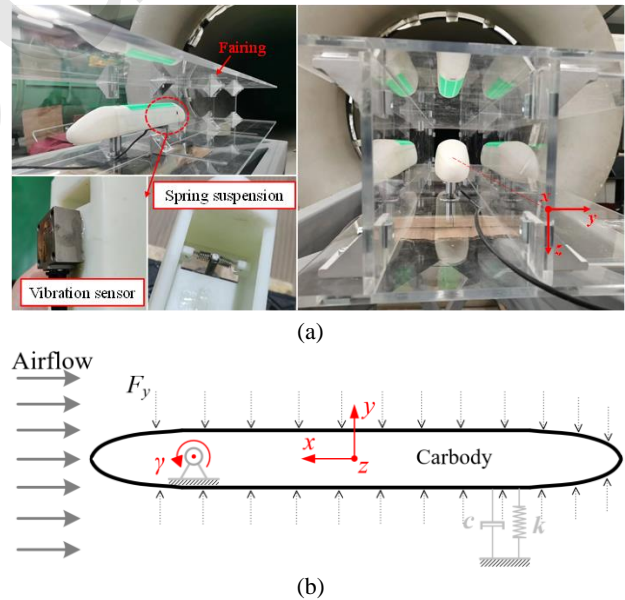
Fig. 13 Train model and wind tunnel: (a) on-site photo; (b) force diagram

The simplified 1/25 train model of the 160 km/h EMU was based on the wind-tunnel experiment conducted by Hemida *et al*. (2009), which consisted of a head dummy attached to the tail vehicle, as

shown in Fig. 13a. In order to make the airflow generated by the open wind tunnel more uniform around the train and facilitate measurement of wind speed, a fairing was added around the train model. The train model was made by 3D printing, and the bogie structure was omitted. The length, width, and height of the train model were 1.2 m, 0.13 m, and 0.16 m, respectively, as shown in Fig. 15. In addition, the train head was fixed to rotate around the *z*-axis, and the train tail could move laterally along the *y*-axis by spring suspension, as shown in Fig. 13b.An acceleration sensor was also installed at the train tail, and the sampling frequency was 1000 Hz. For the whole vehicle dynamics system, the train-tail swaying phenomenon was mainly reflected in the lateral motion *y*, rolling motion *α*, and yawing motion *γ* of the tail carbody. However, when carrying out our simplified wind-tunnel experiment, we only considered the lateral motion *y* of the carbody, so the equation for the lateral dynamics of the train model is as follows:

$$m\ddot{y} + c\dot{y} + ky = F_y. \tag{3}$$

where F_y represents the aerodynamic lateral force acting on the carbody; *m* represents the mass of the train model, which was about 0.2 kg; and the measured lateral stiffness *k* and lateral damping *c* were 500 N/m and 0.8 N s/m, respectively, as illustrated in the ESM. These parameters are also used in the simulation in Section 4.3 below.

Fig. 14 shows the results of the wind-tunnel experiment. The lateral vibration of the train tail was analyzed in the time domain and frequency domain, and the wind speed slowly increased from 0 to 40 m/s (160 km/h) and then decreased to 0. It can be observed that with the increase of wind speed, the maximum amplitude of the vibration acceleration at the train tail reached about 0.5 g. At the same time, the main frequency of the lateral vibration under aerodynamic force is clearly shown to be the natural frequency 8 Hz of the train model. Therefore, we think that the aerodynamic force frequency is dominated by its natural vibration frequency at this time.
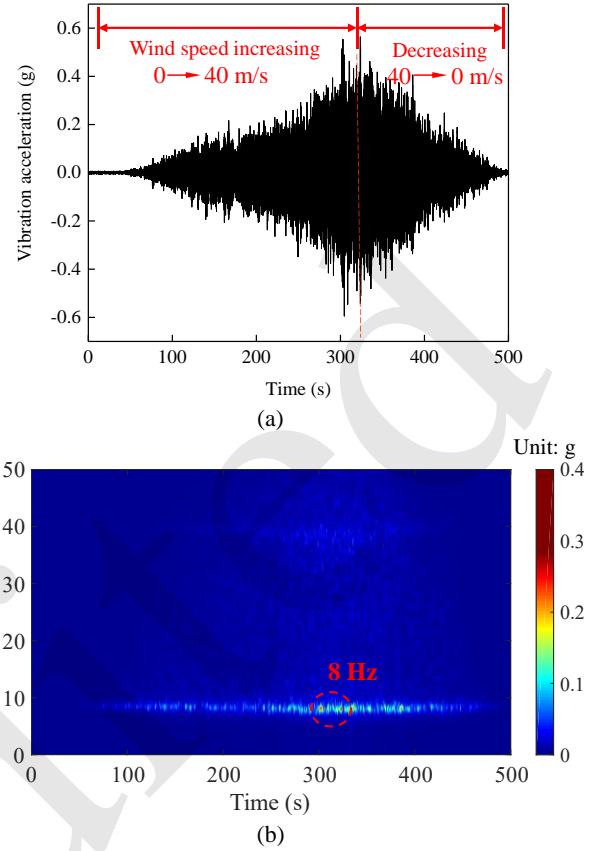
Fig. 14 Lateral acceleration measurement of the train tail: (a) time domain; (b) frequency domain

Unfortunately, due to the limitations of the experimental conditions and scale model, on the one hand, the aerodynamic force was not directly measured, and on the other hand, it was impossible to accurately measure the aerodynamic response of the train tail under the smaller amount of sway. Therefore, the wind-tunnel experiment results are used as a reference for the simulation analysis of the reduced-scale train model in the following section.

4.3 Train scale-model simulation

4.3.1 Modeling and states

The flow field is large in train aerodynamic calculations, which leads to huge computational demands and low computational efficiency. In order to facilitate our research, we therefore conducted numerical calculation on a reduced-scale train model. The simplified 1/25-scale model of the 160 km/h EMU was based on Hemida *et al*. (2009), and was

composed of a head dummy attached to the tail vehicle, as shown in Fig. 15a.

The aerodynamics model of the smaller train is illustrated in Fig. 15b. The width and height of the computational domain are 20h and 12h, respectively. The height of the train model above the ground is 0.05h, as in Li *et al*. (2016). Moreover, the train is located at a distance of 15h from the inlet boundary and 40h from the outlet boundary, which meets the requirement of CEN standards (2010) that the computational domain should extend at least 8 characteristic heights upstream of the train and at least 16 characteristic heights downstream. Furthermore, the inlet boundary is set to velocity inlet with the incoming airflow velocity V, which represents the train speed. The outlet boundary is set to pressure outlet with a reference pressure of 0 Pa. The ground is set as a slip wall, and the slip velocity is the inlet velocity V, in order to simulate the relative motion to the train. The top surface and two side surfaces of the computational domain are defined as the symmetry wall. Finally, the surface of the train has the same parameters as the wall model in Section 2.3.
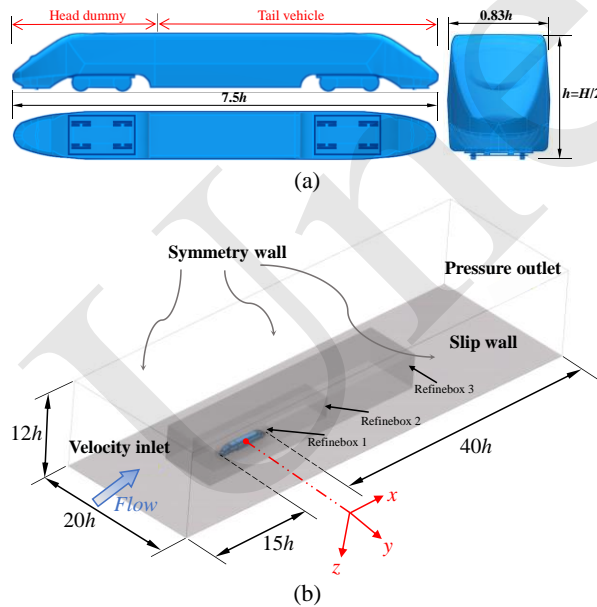
Fig. 15 Aerodynamics model of 1/25-scale train: (a) simplified model based on the 160 km/h EMU; (b) computational domain and boundary conditions

The calculated particle distribution of the computational domain is illustrated in the ESM. In addi-

tion, the calculation time step is set to 0.05 ms, and the independence verification method is the same as described in Section 2.3. The accuracy of the model was further verified by the consistency of the simulation and experimental results given below.

In order to analyze the aerodynamic influence of the train-tail swaying on the wake flow field, we analyzed the aerodynamic performance of the carbody in the following two states:

State 1: Carbody fixed;

State 2: Lateral rigid-body motion (with mass m, stiffness k, and damping c).

State 2 is completely consistent with the wind-tunnel experiment, and a rigid body with a single lateral degree of freedom was built in Simpack, with a mass m of 0.2 kg, stiffness k of 500 N/m, and damping c of 0.8 N s/m. The air density was set to 1.205 kg/m^3 at a standard atmospheric pressure of 101.325 kPa and temperature of 20 ℃. The simulation time was 20 s, in which the velocity V gradually increased from 0 to 40 m/s in the first 10 s, and then gradually decreased to 0; that is, the velocity changed linearly by 4 m/s.
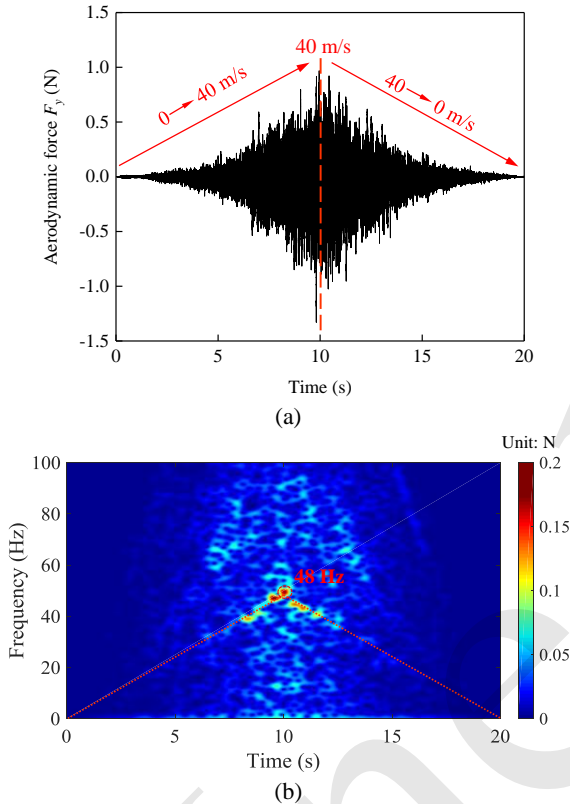
4.3.2 Results and discussion

Fig. 16 displays the results of aerodynamic lateral force in State 1. It can be seen from Fig. 16b that the vortex-induced frequency of the train wake increases linearly with train speed. When the speed reaches 40 m/s (160 km/h), the corresponding vortex-induced frequency is 48 Hz, so it can be calculated that the vortex-induced frequency f_{st} is about 43 Hz at a train speed of 36 m/s (130 km/h). Meanwhile, the calculated $St = f_{st} h/V = 0.188$ is consistent with the results for the real, full-scale train in Section 2, and the vortex-induced frequency is $43/1.7 \approx 25$ times that of the full-scale train, which corresponds to the scale of the model.

Therefore, we can conclude that the vortex-induced frequency of the train wake is only related to train speed and train-tail nose shape. In addition, with increasing train speed, the vortex-induced frequency increases linearly, while it increases inversely with the scale of the train model.

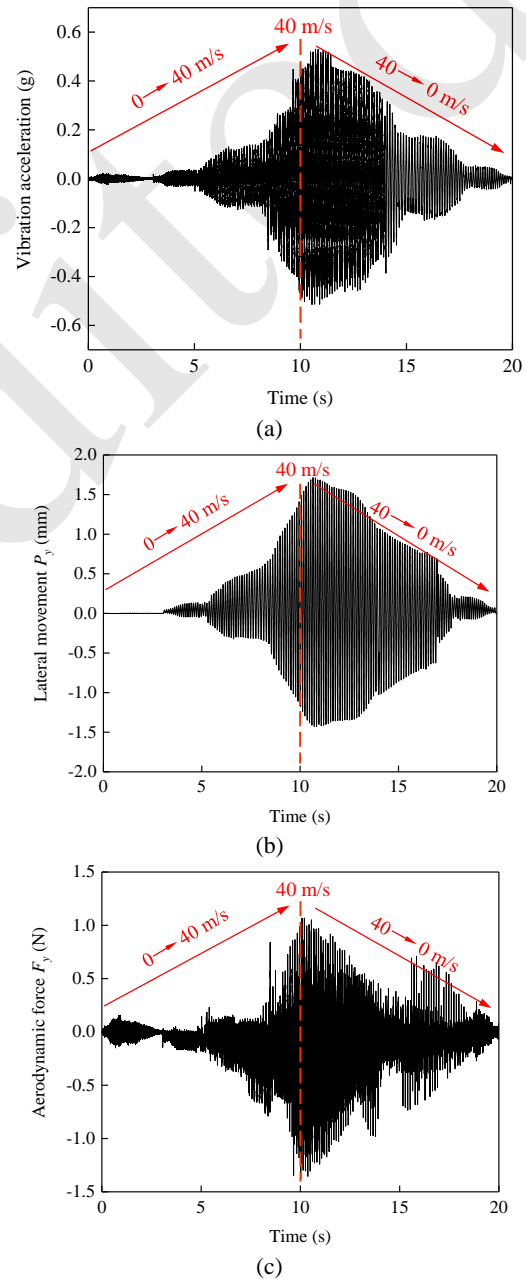In addition, when the train speed V reaches 36

m/s, the corresponding Reynolds number is about 3.88×10^5, which is much larger than the critical Reynolds number 2.5×10^5 of EN 14067-6 (2018). Therefore, the influence of the Reynolds number on the aerodynamic characteristics of the train can be ignored (Tschepe *et al*., 2021).
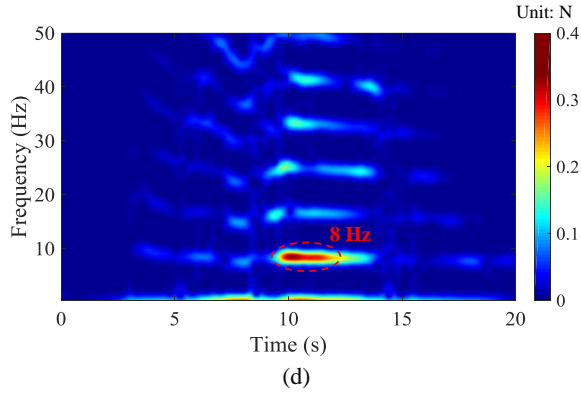
force F_y are shown in Figs. 17c and 17d, respectively. When the train tail sways laterally with a large amplitude, it is evident that the dominant frequency of F_y is the train's natural frequency of 8 Hz, which indicates the occurrence of frequency-locking. However, the value of F_y is obviously different from that in Fig. 16, and our analysis is that the fluid-structure coupling effect changes the vortex-induced frequency of the train wake.

(a)

(b)

Fig. 16 The aerodynamic lateral force F_y in State 1: (a) time domain; (b) frequency domain

Fig. 17 shows the aerodynamic response of the train tail in State 2, including the lateral vibration acceleration, lateral movement P_y, and aerodynamic lateral force F_y. As shown in Fig. 17a, the lateral acceleration amplitude of the train tail is about 0.5g, which is consistent with the wind-tunnel test results in Fig. 14a. Therefore, the accuracy of the simulation model can be verified. It can be observed from Fig. 17b that the amplitude of P_y is about 1.5 mm, corresponding to 1.5 mm $\times 25 = 32.5$ mm for the full-scale train, which is approximately the same as the amplitude of about 25 mm of the EMU train tail shown in Fig. 8a; thus the simulation has certain practical significance as a reference. The time-domain and frequency-domain results of the aerodynamic lateral
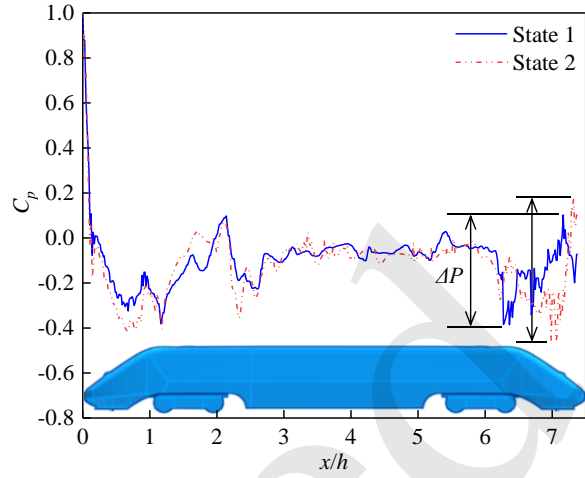

(a)

(b)

(c)

Fig. 17 Aerodynamic responses of the train tail in State 2: (a) Lateral vibration acceleration; (b) Lateral movement P_y; (c) F_y in time domain; (d) F_y in frequency domain

Fig. 18 Cp distribution on the lateral section ($t = 10$ s)

It is certain that the aerodynamic force is caused by the aerodynamic pressure acting on the surface of the carbody, and the aerodynamic pressure distribution on the carbody surface will change significantly when the train tail sways. For ease of comparison, the aerodynamic pressure on the carbody surface is adjusted to be non-dimensional according to the CEN standard (2009a; 2010b), and the normalized aerodynamic pressure coefficient C_p is defined as follows:

$$C_p = (P - P_\infty)/0.5\rho_1 V^2. \tag{4}$$

where P is the static pressure; P_∞ is the reference pressure and is equal to 0 Pa; ρ_1 is the air density, which is set to 1.205 kg/m^3 at the standard atmospheric pressure of 101.325 kPa and a temperature of 20 °C; and the income airflow velocity V is equal to 40 m/s at 10 s.

The lateral pressure distributions on the train surface in the two states are compared in Fig. 18. The horizontal axis is defined as the dimensionless position x/h, where x represents the distance from the front end of the train. It is clear that when the train sways laterally, the C_p distribution at the front end of the train changes slightly, while the C_p distribution at the train tail changes significantly. Specifically, the prominent point of C_p at the train tail obviously moves downstream to the nose tip, and the variation range ΔP of the aerodynamic pressure coefficient increases.

To further explain the influence of train-tail swaying on the aerodynamic pressure on the train surface, we conducted a comparative analysis on the flow field around the train tail in both states. Fig. 19 shows the instantaneous vorticity contour in the z direction at the nose tip of the train tail, and the corresponding time t is 10 s, which is consistent with that in Fig. 18 above. It can be observed from Fig. 22 that the vortices detach from the train tail with high intensity, and the vortex intensity gradually decreases as the vortices flow downstream. In State 1, the high-intensity vortex is separated around the tail nose, as indicated by the red box in Fig. 19a. However, in State 2, the separation point of the high-intensity vortex shifts downstream to the nose tip, as indicated by the red box mark in Fig. 19b. This means that when the carbody is fixed, the aerodynamic frequency is the vortex-induced frequency related to the tail nose shape (see Fig. 16b). When the train tail is swaying severely, the aerodynamic frequency becomes the natural vibration frequency of the train model, which is independent of the aerodynamic shape (see Fig. 17d).
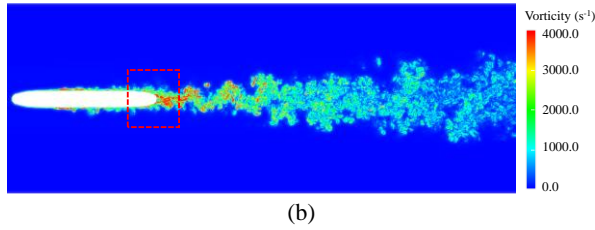

(a)

(b)
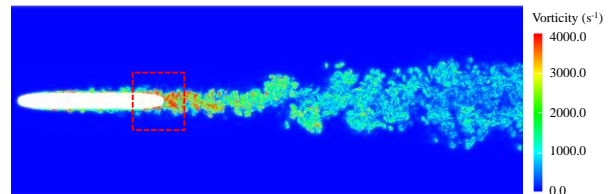
Fig. 19 Contours of the vortices in the z-direction (*t* = 10 s): (a) State 1; (b) State 2

In summary, train-tail swaying affects the flow field of the train wake, and the separation point of the thick turbulent boundary layer on the surface of the train tail moves downstream to the nose tip, thereby changing the vortex-induced frequency. For an EMU operating at 130 km/h, the vortex-induced frequency calculated based on its aerodynamic shape is about 1.7 Hz, which approaches the natural frequency of carbody hunting of 1.3 Hz. In addition, the aerodynamic effect inside a single-line tunnel is strong (the amplitude of F_y reaches 6 kN), which causes vortex-induced vibration (VIV) of the train tail. As the lateral movement of the train tail increases, the vortex-induced frequency shifts from 1.7 Hz to 1.3 Hz, the frequency-locking characteristics of VIV appears, and the resonance causes the train tail to sway continuously in the single-line tunnel.

5. Countermeasures

We pinpointed two fundamental reasons for continuous train-tail swaying of a 160 km/h EMU in a single-line tunnel, through early vehicle development and later experimental research conducted by our research team: First, for the motor vehicle of the train tail, its own primary hunting stability (i.e., carbody hunting) is not enough. Second, the aerodynamic effect in a single-line tunnel is strong, and the periodic vortex-induced force of the train wake leads to vortex-induced vibration of the train tail, which causes resonance of the tail carbody.

In this section, we put forward two main countermeasures for train-tail swaying in single-line tunnels. One is to improve its primary hunting stability through vehicle suspension, and the other is to reduce the aerodynamic vortex shedding force of the train tail by means of aerodynamic shape.

5.1 Optimization of vehicle suspension

Train-tail swaying is part of the carbody hunting motion, which is also called primary hunting motion in the field of railway vehicle dynamics. According to the theory of railway vehicle suspension (Iwnicki *et al.*, 2020), reducing the secondary suspension damping of a vehicle system to within a certain range is beneficial in improving its primary hunting stability. Therefore, we propose Improvement 1, which involves reducing the yaw-damper damping C_{sx} from the normal 800 kN s/m to 600 kN s/m.

In addition, the installation arrangement of the yaw damper is generally divided into two types, called opening outward (OO) and skew symmetry (SS), as illustrated in the ESM. The 160 km/h EMU tail car has a SS yaw-damper arrangement, and there is no doubt that the SS arrangement improves the dynamic performance of the car in some ways. However, as shown in Table 1, when the train operates on the open section (without F_y), the W_y of the front end of the car is 2.08, while the W_y of the rear end is 2.34, indicating that the lateral ride comfort of its rear end is relatively poor; this has been confirmed by Li *et al.* (2022a; 2023b) and Song *et al.* (2023). According to the research of Li *et al.* (2023), the OO arrangement is beneficial in reducing the lateral ride index difference between the two ends of the car. Therefore, we propose Improvement 2, changing the arrangement of the yaw damper from the normal SS to OO.

The dynamic performance of the tail car with Improvements 1 and 2 is shown in Table 1, in which the calculation condition is Cond 2 (see Section 3.1). It can be observed that the W_y of the tail car is 2.34 in the open section (without F_y), but deteriorates to 2.90 in the single-line tunnel (with F_y), which is consistent with the results from the on-track tests (Fig. 11b). In addition, we measured the W_y of the train tail with each improvement separately, and found that with Improvements 1 and 2, the W_y of the train tail is 2.74 and 2.72, respectively, both of which are at the excellent level (less than 2.75), indicating that these two improvements to the yaw damper can effectively alleviate train-tail swaying in a single-line tunnel.

Table 1 Vehicle dynamic performance (without/with aerodynamic force F_y)

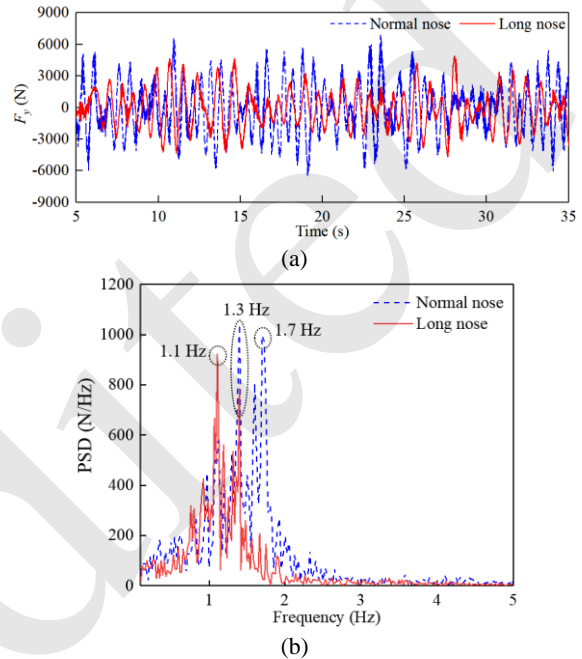| Vehicle suspension	Yaw damper damping C_{xx} (kN s/m)	Yaw damper arrangement	Lateral ride comfort W_y	
			Front-end	Rear-end
Normal	800	SS	2.08 / 2.13	2.34 / **2.90**
Improvement 1	600	SS	2.05 / 2.11	2.26 / 2.74
Improvement 2	800	OO	2.14 / 2.17	2.15 / 2.72

5.2 Optimization of aerodynamic shape

A good streamlined carbody shape is beneficial in reducing aerodynamic resistance during train operation. Because of the vortex-shedding characteristics of the train wake, the high-intensity vortices mainly detach from the tail nose. Therefore, on the basis of the original carbody shape, we only changed the aerodynamic shape of the tail nose and extended it by 0.4H along the x-axis, as shown in Fig. 20.
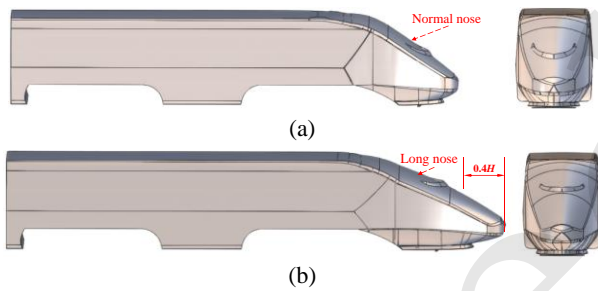
Fig. 20 Aerodynamic optimization of the train-tail nose shape: (a) normal nose; (b) long nose

Fig. 21 The aerodynamic vortex-induced force F_y of the train tail under Cond 2: (a) time domain; (b) frequency domain

Fig. 21 shows the aerodynamic vortex-induced force F_y of the train tail with two different nose shapes, with calculation conditions Cond 2. The F_y amplitude of the long-nose train is about 5 kN, and the vortex-induced frequency is 1.1 Hz. In addition, compared with the normal short-nose train, the W_y of the train tail of the long-nose carbody is reduced from 2.9 to 2.65.

Referring to Hemida *et al*.'s research (2010a; 2014b), we found that the wake of the short-nose train shows more high-intensity vortex structures than that of the long-nose train. We believe that compared with the short-nose vehicle, the long-nose train reduces the amplitude of aerodynamic vortex-induced force of the train tail, and also decreases vortex-induced frequency.

For an EMU operating at 130 km/h, the long-nose carbody will cause the vortex-induced frequency to decrease from 1.7 Hz to 1.1 Hz, although it is closer to the carbody hunting frequency of 1.3 Hz. However, the amplitude of the aerodynamic vortex-induced force F_y will be reduced from 6 kN to 5 kN (17%), thus greatly weakening the aerodynamic effect and improving the lateral ride comfort of the train tail running in a single-line tunnel.

5 Conclusions

Aiming to improve train-tail swaying of 160 km/h EMUs in single-line tunnels, which is an urgent on-site problem, we studied the aerodynamic performance of the train tail by experiments and simulations. The influence mechanism of train-tail swaying on train-wake characteristics was revealed. This

permitted us to suggest countermeasures for train-tail swaying in single-line tunnels, with regard to two key aspects. The major conclusions of this study are as follows:

(1) When the train tail sways with a small amplitude (within 10 mm), its aerodynamic force frequency (i.e., vortex-induced frequency) is about 1.7 Hz at 130 km/h, which is related to train speed and the nose shape of the train tail. At higher train speeds, the vortex-induced frequency of the train wake increases linearly. In addition, when the tail nose is extended, the vortex-induced frequency decreases.

(2) As the swaying amplitude of the train tail increases (exceeding 25 mm), the separation point of the high-intensity vortex in the train wake shifts downstream to the nose tip, thereby changing the vortex-induced frequency from 1.7 Hz to the nearby carbody hunting frequency of 1.3 Hz. This suggests that the frequency-locking characteristic appears, and the resonance caused by vortex-induced vibration (VIV) intensifies train-tail swaying.

(3) For the motor vehicle of the train tail, adopting an opening outward (OO) arrangement for the yaw damper or reducing yaw-damper damping within a certain range can effectively weaken train-tail swaying inside single-line tunnels. In addition, when the tail nose is extended, the amplitude of the vortex-induced force is reduced, thereby weakening the aerodynamic effect and solving the problem of train-tail swaying inside single-line tunnels.

Author contributions

Yuan YAO designed the research. Yadong SONG and Longjiang SHEN processed the corresponding data. Yadong SONG wrote the first draft of the manuscript. Yanpeng ZOU and Ting QIN helped to organize the manuscript. Yuan YAO revised and edited the final version.

Conflict of interest

Yadong SONG, Yanpeng ZOU, Yuan YAO, Ting QIN, and Longjiang SHEN declare that they have no conflict of interest.

References

Bell JR, Burton D, Thompson MC, et al., 2014. Wind tunnel analysis of the slipstream and wake of a high-speed train. *Journal of Wind Engineering and Industrial Aerodynamic*, 134:122-138.
https://doi.org/10.1016/j.jweia.2014.09.004

Bell JR, Burton D, Thompson MC, et al., 2015. Moving model analysis of the slipstream and wake of a high-speed train. *Journal of Wind Engineering and Industrial Aerodynamic*, 136:127-137.
https://doi.org/10.1016/j.jweia.2014.09.007

Bell JR, Burton D, Thompson MC, et al., 2016. Dynamics of trailing vortices in the wake of a generic high-speed train. *Journal of Fluids and Structures*, 65:238-256.
https://doi.org/10.1016/j.jfluidstructs.2016.06.003

Bell JR, Burton D, Thompson MC, et al., 2016. Flow topology and unsteady features of the wake of a generic high-speed train. *Journal of Fluids and Structures*, 61:168-183.
https://doi.org/10.1016/j.jfluidstructs.2015.11.009

BS EN (British Standard Institute, London), 2018, Railway Applications–Aerodynamics Part 6: Requirements and Test Procedures for Crosswind Assessment, no. 14067-6.

CEN European Standard. 2009. Railway applications-aerodynamics. Part 4: requirements and test procedures for aerodynamics on open track, CEN EN 14067-4.

CEN European Standard. 2010. Railway applications-aerodynamics. Part 6: requirements and test procedures for cross wind assessment, CEN EN 14067-6.

Choi JK, Kim KH, 2014. Effects of nose shape and tunnel cross-sectional area on aerodynamic drag of train traveling in tunnels. *Tunnelling and Underground Space Technology incorporating Trenchless Technology Research*, 41:62-73.
https://doi.org/10.1016/j.tust.2013.11.012

Diedrichs B, Berg M, Stichel S, et al., 2007. Vehicle dynamics of a high-speed passenger car due to aerodynamics inside tunnels. *Proceedings of the Institution of Mechanical Engineers Part F Journal of Rail and Rapid Transit*, 221(4):527-545.
https://doi.org/10.1243/09544097JRRT125

Diedrichs B, Krajnović S, Berg M, 2008. On the aerodynamics of car body vibrations of high-speed trains cruising inside tunnels. *Engineering Applications of Computational Fluid Mechanics*, 2(1):51-57.
https://doi.org/10.1080/19942060.2008.11015211

Du JM, Fang Q, Wang G, et al., 2022. Aerodynamic effects produced by a high-speed train traveling through a tunnel considering different car numbers. *Symmetry-Basel*, 14(3):479.
https://doi.org/10.3390/sym14030479

Fujimoto H, Miyamoto M, Shimamoto Y, 1993. Lateral vibration and its decreasing measure in the tail car of a

Shinkansen. *Transactions of the Japan Society of Mechanical Engineers*, 59(560):1016-1022.
https://doi.org/10.1299/kikaic.59.1016

National Railway Administration, 2020. Gauge for standard gauge railways Part 2: Structure gauge, GB 146.2-2020. National Standards of People's Republic of China (in Chinese).

Hemida H, Krajnovic S, 2009. Exploring flow structures around a simplified ICE2 train subjected to a 30 degrees side wind using LES. *Engineering Applications of Computational Fluid Mechanics*, 3(1):28-41.
https://doi.org/10.1080/19942060.2009.11015252

Hemida H, Krajnovic S, 2008. LES Study of the influence of a train-nose shape on the flow structures under cross-wind conditions. *Journal of Fluids Engineering-transactions of the Asme*, 130(9):091101.
https://doi.org/10.1115/1.2953228

Hemida H, Baker C, Gao G, 2014. The calculation of train slipstreams using large-eddy simulation. *Proceedings of the Institution of Mechanical Engineers Part F Journal of Rail and Rapid Transit*, 228(1):25-36.
https://doi.org/10.1177/095440971246098

Han P, deLangre E, Thompson MC, et al., 2023. Vortex-induced vibration forever even with high structural damping. *Journal of Fluid Mechanics*, 962:A13.
https://doi.org/10.1017/jfm.2023.268

Iwnicki S, Spiryagin M, Cole C, et al., 2020. Handbook of railway vehicle dynamics. 2nd ed. Boca Raton (FL): CRC Press.

Khier W, Breuer M, Durst F, 2000. Flow structure around trains under side wind conditions: a numerical study. *Computers & Fluids*, 29(2):179-195.
https://doi.org/10.1016/S0045-7930(99)00008-0

Kikko S, Tanifuji K, Sakanoue K, et al., 2008. Modeling of aerodynamic force acting in tunnel for analysis of riding comfort in a train. *Journal of Mechanical Systems for Transportation and Logistics*, 1(1):31-42.
https://doi.org/10.1299/jmtl.1.31

Li JY, Liu LY, Kou DH, 2014. Wu Guang high-speed rail track irregularity power spectrum analysis. *Applied Mechanics & Materials*, 638-640:1224-1228.
https://doi.org/10.4028/www.scientific.net/AMM.638-640.1224

Li L, Liu TH, Guo ZJ, et al., 2021. On the effect of rail-end slope in train aerodynamics under crosswind. *Vehicle System Dynamics*, 60(6):1888-1908.
https://doi.org/10.1080/00423114.2021.1883067

Li T, Dai ZY, Yu MG, et al., 2021. Numerical investigation on the aerodynamic resistances of double-unit trains with different gap lengths. *Engineering Applications of Computational Fluid Mechanics*, 15(1):549-560.
https://doi.org/10.1080/19942060.2021.1895321

Li T, Hao L, Jie Z, et al., 2023. Numerical study on aerodynamic resistance reduction of high-speed train using vortex generator. *Engineering Applications of Computational Fluid Mechanics*, 17(1):e2153925.
https://doi.org/10.1080/19942060.2022.2153925

Liu DJ, Li XZ, Mei FL, et al., 2022. Effect of vertical vortex-induced vibration of bridge on railway vehicle's running performance. *Vehicle System Dynamics*, 61(5):1432-1447.
https://doi.org/10.1080/00423114.2022.2084120

Li W, Guan QH, Chi MR, et al., 2022. An investigation into the influence of wheel-rail contact relationships on the carbody hunting stability of an electric locomotive. *Proceedings of the Institution of Mechanical Engineers Part F Journal of Rail and Rapid Transit*, 236(10):1198-1209.
https://doi.org/10.1177/0954409722108441

Li G, Wu RD, Deng XX, et al., 2022. Suspension parameters matching of high-speed locomotive based on stability/comfort Pareto optimization. *Vehicle System Dynamics*, 60(11):3848-3867.
https://doi.org/10.1080/00423114.2021.1979602

Li G, Zhou Y, Yuan Yao, et al., 2022. Application of yaw dampers with frequency-selective damping to improve the locomotive adaptability to low/high conicity stability. *Proceedings of the Institution of Mechanical Engineers Part F Journal of Rail and Rapid Transit*, 237(6):784-795.
https://doi.org/10.1177/09544097221141517

Li G, Yao Y, Shen LJ, et al., 2023. The influence of yaw damper layouts on locomotive lateral dynamics performance: Pareto optimization and parameter analysis. *Journal of Zhejiang University-SCIENCE A*, 24(5):450-464.
https://doi.org/10.1631/jzus.A2200374

Niu JQ, Liang XF, Zhou D, 2016. Experimental study on the effect of Reynolds number on aerodynamic performance of high-speed train with and without yaw angle. *Journal of Wind Engineering and Industrial Aerodynamics*, 157:36-46.
https://doi.org/10.1016/j.jweia.2016.08.007

Niu JQ, Zhou D, Liu TH, et al., 2017. Numerical simulation of aerodynamic performance of a couple multiple units high-speed train. *Vehicle System Dynamics*, 55(5):681-703.
https://doi.org/10.1080/00423114.2016.1277769

Niu JQ, Zhou D, Liang XF, et al., 2018. Numerical simulation of the Reynolds number effect on the aerodynamic pressure in tunnels. *Journal of Wind Engineering and Industrial Aerodynamics*, 173:187-198
https://doi.org/10.1016/j.jweia.2017.12.013

National Railway Administration, 2019. Specification for dynamics performance assessment and testing verification of rolling stock, GB/T 5599. National Standards of People's Republic of China (in Chinese).

Pan YC, Yao JW, Liu T, et al., 2018. Discussion on the wake vortex structure of a high-speed train by vortex identification methods. *Lixue Xuebao/Chinese Journal of Theoretical and Applied Mechanics*, 50(3): 667-676. (in Chinese).
https://doi.org/10.6052/0459-1879-17-383

Suzuki M, 2000. Aerodynamic force acting on train in tunnel. *RTRI Report*, 14(9):37-42. (In Japanese).

Suzuki M, 2001. Unsteady aerodynamic force acting on high speed trains in tunnel. *Quarterly Report of RTRI*, 42(2):89-93.
https://doi.org/10.2219/rtriqr.42.89

Suzuki M, 2004. Flow-induced vibration of high-speed trains in tunnels. *The Aerodynamics of Heavy Vehicles: Trucks, Buses, and Trains*, 19:443-452.
https://doi.org/10.1007/978-3-540-44419-039

Schulte-Werning B, Heine C, Matschke G, 2003. Unsteady Wake Flow Characteristics of High-Speed Trains. *Proceedings in Applied Mathematics and Mechanics*, 2(1):332-333.
https://doi.org/10.1002/pamm.200310150

Shi YX, Dai HY, Wang QS, et al., 2020. Research on low-frequency swaying mechanism of metro vehicles based on wheel-rail relationship. *Shock and Vibration*, 2020:8878020.
https://doi.org/10.1155/2020/8878020

Sun JF, Chi MR, Jin XS, et al., 2021. Experimental and numerical study on carbody hunting of electric locomotive induced by low wheel-rail contact conicity. *Vehicle System Dynamics*, 59(2):203-223.
https://doi.org/10.1080/00423114.2019.1674344

SIMULIA Inc, SIMULIA Xflow User's Guide, Release 2021x.

Song YD, Qin T, Yao Y, et al., 2023. Investigation on aerodynamic fluid-structure coupling vibration of 160 km/h EMU tail in single-track tunnels. *International Journal of Structural Stability and Dynamics*.
https://doi.org/10.1142/S0219455424501979

Takai H, 1990. Maintenance of track with long-wave track irregularity on Shinkansen. *Railway Technical Research Institute Quarterly Reports*, 3:13–20.

Tanifuji K, Sakanoue K, Kikko S, 2008. Modelling of aerodynamic force acting on high speed train in tunnel and a measure to improve the riding comfort utilising restriction between cars. *Vehicle System Dynamics*, 46(S1):1065-1075.
https://doi.org/10.1080/00423110802158747

Tschepe J, Nayeri CN, Paschereit CO, et al., 2021. On the influence of Reynolds number and ground conditions on the scaling of the aerodynamic drag of trains. *Journal of Wind Engineering and Industrial Aerodynamics*, 213:104594.
https://doi.org/10.1016/j.jweia.2021.104594

Williamson CH, Govardhan R, 2004.Vortex-induced vibration. *Annual Review of Fluid Mechanics*, 36(1):413-455.
https://doi.org/10.1146/annurev.fluid.36.050802.122128

Wu H, Zeng XH, Lai J, et al., 2020. Nonlinear hunting stability of high-speed railway vehicle on a curved track under steady aerodynamic load. *Vehicle System Dynamics*, 58(2):175-197.
https://doi.org/10.1080/00423114.2019.1572202

Wang JC, Ling L, Ding X, et al., 2022. The influence of aerodynamic loads on carbody low-frequency hunting of high-speed trains. *International Journal of Structural Stability and Dynamics*, 22(13):2250145.

https://doi.org/10.1142/S0219455422501450

Yao SB, Sun ZX, Guo DL, et al., 2013. Numerical study on wake characteristics of high-speed trains. *Acta Mechanica Sinica*, 29(6):811-822.
https://doi.org/10.1007/s10409-013-0077-3

Yao Y, Xu G, Song YD, et al., 2021. Mechanism of train tail lateral sway of EMUs in tunnel based on vortex-induced vibration. *Journal of Traffic and Transportation Engineering*, 21(5):51-61(in Chinese).
https://doi.org/10.19818/j.cnki.1671-1637.2021.05.010

Yu HY, Oiseth O, Zhang MJ, et al., 2023. Tuned mass damper design for vortex-induced vibration control of a bridge: influence of vortex-induced force model. *Journal of Bridge Engineering*, 28(5):04023021.
https://doi.org/10.1061/JBENF2.BEENG-5958

Zhou L, Ge YJ, 2008. Wind tunnel test for vortex-induced vibration of vehicle-bridge system section model. *Journal of the Brazilian Society of Mechanical Sciences and Engineering*, 30(2):110-117.
https://doi.org/10.1590/S1678-58782008000200003

Zeng XH, Wu H, Lai J, et al., 2014. Influences of aerodynamic loads on hunting stability of high-speed railway vehicles and parameter studies. *Acta Mechanica Sinica*, 30(6):889-900.
https://doi.org/10.1007/s10409-014-0119-5

Zeng XH, Lai J, Wu H, 2018. Hunting stability of high-speed railway vehicles under steady aerodynamic loads. *International Journal of Structural Stability and Dynamics*, 18(7):1850093.
https://doi.org/10.1142/S0219455418500931

Zhao X, Tan M, Zhu WD, et al., 2023. Study of Vortex-Induced Vibration of a Pipe-in-Pipe System by Using a Wake Oscillator Model. *Journal of environmental engineering*, 149(4):04023007.
https://doi.org/10.1061/JOEEDU.EEENG-7178

Zhang GQ, Xu YL, Wang B, et al., 2023. Turbulence Effects on Vortex-Induced Dynamic Response of a Twin-Box Bridge and Ride Comfort of the Vehicle. *International Journal of Structural Stability and Dynamics*, 23(16n18):2340023.
https://doi.org/10.1142/S0219455423400230

Electronic supplementary materials

Section S1–S6, Table S1, Figs. S1–S5

中文概要

题　目：单线隧道内列尾晃车的空气动力学及对策研究

作　者：宋亚东 [1]，邹延鹏 [2]，姚远 [1,3⊠]，秦汀 [1]，沈龙江 [3]

机　构：[1]西南交通大学，轨道交通运载系统全国重点实验室，中国成都，610031；[2]中国中车长客股份有限公司基础服务部，中国长春，130062；[3]中国中车

株洲电力机车有限公司重载、高速大功率电力机车国家重点实验室，中国株洲，412000

目　的： 近年来，正在运营的 160 km/h 动力集中动车组在单线隧道内列尾晃车问题突出，亟待解决。本文旨在通过仿真与试验分析，来研究列尾晃车的机理及气动特征，并提出有效的解决措施。

创新点： 1. 建立了尾车流固耦合振动的仿真模型，复现了单线隧道内列尾的气动晃车现象，并对其气动特征展开了研究；2. 通过现场试验和比例模型风洞实验，验证了列尾晃车的涡激共振机理。

方　法： 1. 通过现场试验，测得了该实际运营的动车组通过单线隧道时列尾的晃车频率；2. 通过尾车流固耦合振动的仿真分析，阐明了列尾的气动晃车机理及影响因素，并提出了缓解措施；3. 通过列车比例模型的风洞实验与仿真分析，再次验证了列尾涡激共振的晃车机理。

结　论： 1. 列尾脱涡力频率与尾鼻外型及列车运行速度有关，且随着列车速度的增加而线性增大；2. 对于该动力集中动车组，在 130 km/h 速度下运行时，列尾的气动脱涡力频率为 1.7 Hz，随着列尾晃车幅值的增加，脱涡力频率变为附近 1.3 Hz 的车体蛇行频率，表明出现了涡激振动的锁频特性，涡激共振导致了列尾的剧烈晃车现象；3. 对于列尾动力车，通过抗蛇行减振器改进或尾鼻外型优化，两种措施均可有效改善列尾在单线隧道内的气动晃车问题。

关键词： 列尾晃车；涡激振动；列车尾流；列车空气动力学；车辆系统动力学